



Cycle Life Modeling of Lithium-Ion Batteries

Gang Ning* and Branko N. Popov**^z

Department of Chemical Engineering, University of South Carolina, Columbia, South Carolina 29208, USA

A first-principles-based charge-discharge model was developed to simulate the capacity fade of Li-ion batteries. The model is based on the loss of active lithium ions due to solvent reduction reaction and on the rise of the anode film resistance. The effect of parameters such as exchange current density, depth of discharge (DOD), end of charge voltage, film resistance, and the overvoltage of parasitic reaction were studied quantitatively. The model controls the required DOD by controlling the discharge time and estimates the end of discharge voltages as a function of cycle number.

© 2004 The Electrochemical Society. [DOI: 10.1149/1.1787631] All rights reserved.

Manuscript submitted December 30, 2003; revised manuscript received March 12, 2004. Available electronically September 21, 2004.

Accelerated cycle life testing and developing correlations based on this data are critical for the capacity fade evaluation of batteries.¹⁻³ Darling and Newman⁴ made a first attempt to model the parasitic reactions in lithium-ion batteries by incorporating a solvent oxidation into a lithium-ion battery model. Spotnitz⁵ developed polynomial expressions for estimation of irreversible and reversible capacity loss due to solid electrolyte interphase (SEI) film growth and dissolution in lithium-ion batteries. Ramadass *et al.*⁶ developed a capacity fade prediction model for Li-ion cells based on a semi-empirical approach. Recently, Christensen and Newman⁷ simulated the influence of the anode film resistance on the charge/discharge performance of a lithium-ion battery. In this model the loss of reversible lithium ions and increase in the anode film resistance were incorporated into the first-principles model developed by Doyle *et al.*⁸ Process parameters such as charge rate (CR), the depth of discharge (DOD), end-of-charge voltage (EOCV), and the discharge rate (DR) which influence the capacity fade⁹ were not considered in the above-mentioned models.

We developed a first-principles-based model to simulate the capacity fade of Li-ion batteries in which incorporation of a continuous occurrence of the solvent reduction reaction during constant current and constant voltage (CC-CV) charging explains the capacity fade of the battery.¹⁰ Initially the model estimates the capacity fade parameters as a function of cycle number. Next it is necessary to run the lithium-ion intercalation model with the updated parameters to estimate the performance of the battery at a specific cycle number. However, to run both models takes a long computational time. Also, the model does not consider the discharge process, which leads to inaccurate estimation of the total reaction time for the parasitic reaction.

In this paper, a charge-discharge capacity fade model was developed based on the loss of active lithium ions due to solvent reduction reaction. The rise of the surface film resistance at the anode due to the parasitic reaction occurring was also considered in the model. The model considers process parameters such as: CR, DOD, EOCV, and the DR. It controls the required DOD by controlling the discharge time and estimates the discharge voltage as a function of cycle number. To decrease the computational time, the transport of lithium in the liquid phase was neglected. It takes only 10 h using a computer with 2.0 GHz CPU and 512 Mb RAM to run the model and to estimate the capacity fade and the charge-discharge performance of a battery cycled up to 2000 times.

Model Development

The simulations were carried out based on the experimental data obtained for a pouch lithium-ion cell (2.187 Ah), which consists of Li_xCoO_2 positive electrode and mesocarbon microbead (MCMB) negative electrode.

The charge-discharge simulations were performed by using a direct charge current of 0.334 A to a specified EOCV of 4.0 or 4.2 V. Next, the voltage was held constant until the charge current decreased to 50 mA. Subsequently, the battery was discharged under a direct current of 0.835 A to a specified DOD of 0.4 or 0.6. There was no rest time between charging and discharging.

For simulation of the capacity check, the battery was initially discharged using a discharge current of 0.835 A to 3.0 V. Next, the battery was charged by applying a conventional CC-CV protocol (0.334 A to 4.2 V with a 50 mA cutoff current). The fully charged battery was discharged for second time to 3.0 V. The value of discharge capacity estimated in the second discharge process was used for capacity fade analysis. Both charge-discharge and the capacity check simulations terminate when the battery reaches a voltage lower than 3.0 V.

As shown in Fig. 1, during discharge, the lithium ions deintercalate from the negative electrode and intercalate into the positive electrode. Inside the porous electrode, the intercalation/deintercalation processes take place at the electrode/electrolyte interface. A rigorous model based on porous electrode theory, concentrated solution theory, Ohm's law, and intercalation/deintercalation kinetics was developed previously which simulates the galvanostatic charge/discharge behavior of a Li-ion rechargeable battery.⁸ In the model suggested in this paper, the variation of Li^+ concentration in the liquid phase along the current path was neglected because low-to-medium charge/discharge currents were used in the simulations. The variation in the solid phase potential at the anode or at the cathode is negligible because of good conductivity of the electrode materials. It was also assumed that the active electrode materials are made from uniform spherical particles with a radius of R_i and that the diffusion is the only mechanism of lithium transport inside the particles. The direction normal to the surface of the particles was taken to be the r -direction. The model equation that describes the diffusion of lithium in the solid phase is given by Fick's 2nd law

$$\frac{\partial C_i^{\text{Li}}}{\partial t} = \frac{D_i^1}{(r_i)^2} \frac{\partial}{\partial r_i} \left(r_i^2 \frac{\partial C_i^{\text{Li}}}{\partial r_i} \right), \quad i = n, p \quad [1]$$

The initial condition is

$$C_i^{\text{Li}} = C_{i0}^{\text{Li}} \quad \text{at } t = 0, \quad i = n, p \quad [2]$$

The boundary conditions for constant current charge/discharge are

$$r_i = 0, \quad t > 0, \quad \frac{\partial C_i^{\text{Li}}}{\partial r_i} = 0, \quad i = n, p \quad [3]$$

and

$$r_i = R_i, \quad t > 0, \quad D_i^1 \frac{\partial C_i^{\text{Li}}}{\partial r_i} = \frac{-J_i^{\text{Li}}}{F}, \quad i = n, p \quad [4]$$

* Electrochemical Society Student Member.

** Electrochemical Society Active Member.

^z E-mail: popov@enr.sc.edu

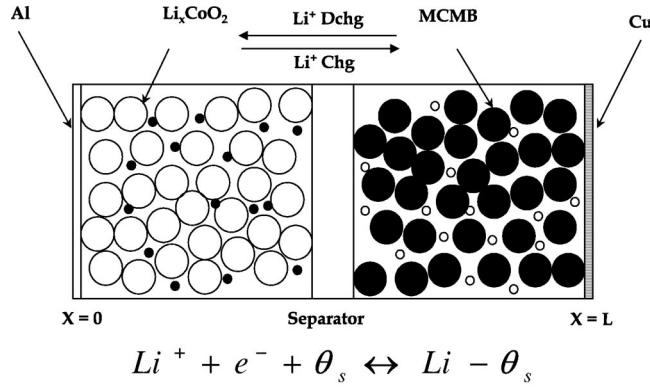


Figure 1. Schematic of a rechargeable Li-ion battery.

where J_i^{Li} is the average local reaction (intercalation/deintercalation) current density defined as

$$J_i^{\text{Li}} = \frac{I_i}{S_i}, \quad i = n, p \quad [5]$$

where S_i is the superficial surface area, related to the volume of the electrode through the specific surface area by

$$S_i = a_i V_i, \quad i = n, p \quad [6]$$

The specific surface area, a_i is given by

$$a_i = \frac{3\varepsilon_i}{R_i}, \quad i = n, p \quad [7]$$

I_i is the total intercalation/deintercalation current.

Butler-Volmer (BV) kinetics was used to describe lithium intercalation/deintercalation

$$J_i^{\text{Li}} = J_{i0}^{\text{Li}} \left\{ \exp\left(\frac{\alpha_i^a F}{RT} \eta_i\right) - \exp\left(\frac{-\alpha_i^c F}{RT} \eta_i\right) \right\}, \quad i = n, p \quad [8]$$

J_{i0}^{Li} , the concentration-dependent exchange current density, is given by

$$J_{i0}^{\text{Li}} = k_i (c_i^{\text{max}} - C_i^{\text{Li-S}})^{\alpha_i^a} (C_i^{\text{Li-S}})^{\alpha_i^c} (C_{\text{Li}^+})^{\alpha_i^c}, \quad i = n, p \quad [9]$$

$C_i^{\text{Li-S}}$ is the solid phase lithium concentration at the electrode/electrolyte interface calculated using Eq. 1-4. The overpotential term in Eq. 8 is given by

$$\eta_i = \phi_i^1 - \phi_i^2 - U_i^{\text{OCP}} - J_i S_i R_i^f, \quad i = n, p \quad [10]$$

where J_i is the total faradaic current across the SEI. Variation of ϕ_2 (the liquid phase potential) along the current path was neglected due to low charge/discharge currents used to simulate the charge-discharge cycling and was arbitrarily set to zero. Thus, Eq. 10 is simplified to

$$\eta_i = \phi_i^1 - U_i^{\text{OCP}} - J_i S_i R_i^f, \quad i = n, p \quad [11]$$

Equation 2-4 are still valid as boundary conditions for CV charging stage. In addition, the following condition was used to solve for the continued current decay

$$\phi_p^1 - \phi_n^1 = 4.0/4.2 \text{ V} \quad [12]$$

Equation 1-4 were transformed into dimensionless form

$$\frac{\partial \bar{C}_i^{\text{Li}}}{\partial \bar{t}} = \frac{1}{\bar{r}_i^2} \frac{\partial \bar{r}_i}{\partial \bar{r}_i} \left(\bar{r}_i^2 \frac{\partial \bar{C}_i^{\text{Li}}}{\partial \bar{r}_i} \right), \quad i = n, p \quad [13]$$

Initial condition

$$\bar{C}_i^{\text{Li}} = \bar{C}_{i0}^{\text{Li}} \quad \text{at } \bar{t} = 0, \quad i = n, p \quad [14]$$

Boundary conditions

$$\bar{r}_i = 0, \quad \bar{t} > 0, \quad \frac{\partial \bar{C}_i^{\text{Li}}}{\partial \bar{r}_i} = 0, \quad i = n, p \quad [15]$$

and

$$\bar{r}_i = 1, \quad \bar{t} > 0, \quad \frac{C_i^{\text{max}} D_i^1}{R_i} \frac{\partial \bar{C}_i^{\text{Li}}}{\partial \bar{r}_i} = \frac{-J_i^{\text{Li}}}{F}, \quad i = n, p \quad [16]$$

where

$$\bar{C}_i^{\text{Li}} = \frac{C_i^{\text{Li}}}{C_i^{\text{max}}}, \quad \bar{r}_i = \frac{r_i}{R_i}, \quad \bar{t} = \frac{t D_i^1}{R_i^2}, \quad i = n, p \quad [17]$$

The open circuit potential U_i^{OCP} is a function of the lithium concentration in the solid phase of the particles ($C_i^{\text{Li-S}}$). The U_i^{OCP} was estimated by fitting the experimental low-rate ($C/20$ rate) charge/discharge voltage profile of the positive and negative electrode. The experimental charge-discharge curves were obtained by charging and discharging the cathode and anode material in T-cell configuration.⁹

$C_i^{\text{Li-S}}$, the dimensionless solid phase lithium concentration at the electrode/electrolyte interface is defined as

$$\bar{C}_i^{\text{Li-S}} = \frac{C_i^{\text{Li-S}}}{C_i^{\text{max}}}, \quad i = n, p \quad [18]$$

The carbon electrode, when polarized to low potential during charging, reduces the electrolyte to insoluble salts, resulting in formation of a new surface film similar to the surface film formed during the formation period.¹¹⁻¹³ It is generally assumed that the surface film formed on carbon electrode may not be able to fully accommodate the volume change of graphite particles due to intercalation/deintercalation of lithium or due to accumulation of gaseous by-products. A continuous small-scale reduction can take place on the negative electrode when the solvent percolates through the cracks of the surface film. A part of lithium is irreversibly lost due to this parasitic reaction. The following assumptions with regard to the parasitic reactions were made in this model

1. The reduction of ethylene carbonate (EC) was chosen to be the parasitic reaction occurring at the negative electrode/electrolyte interface



2. The EC reduction takes place on the negative electrode at an overpotential which is more cathodic than the reversible potential of the parasitic reaction. No parasitic reaction was considered on the surface of Li_xCoO_2 electrode at any time.

3. The total surface film resistance (R^f) consists of initial film resistance (R_C) and the resistance of the film formed as a result of the parasitic reaction occurring at the anode surface (R_S). The thickness of the film at the negative electrode increases with cycling. Initially only R_C exists

$$R^f = R_C + R_S \quad [20]$$

Table I. Electrode parameters for the cycle life modeling of a rechargeable Li-ion battery.

Parameter	Units	Anode (MCMB)	Cathode (Li _x CoO ₂)
V_i	cm ³	7.368	6.221
ε_i		0.49	0.59
C_i^{\max}	mol/cm ³	3.0555×10^{-2}	5.1555×10^{-2}
D_i^e	cm ² /s	3.8×10^{-10}	1.0×10^{-9}
α_i^a/α_i^c		0.5/0.5	0.5/0.5
r_i	cm	2.0×10^{-4}	2.0×10^{-4}
k_i	$\frac{\text{A/cm}^2}{(\text{mol/cm}^3)^{0.5}}$	8.351×10^{-4}	6.374×10^{-4}
$R_{\text{filN}=0}$ or R_{SEI}	mΩ	20	0
$C_{\text{Li}^+}^{\text{L}}$	mol/cm ³		1.0×10^{-3}

4. The open circuit potential (OCP) or equilibrium potential for the EC reduction was chosen to be 0.4 V (vs. Li⁺/Li).^{10,13,14} The electrolyte reduction reaction is irreversible.

Because the concentration variation in liquid phase was neglected, the current density of the parasitic reaction is given by the Tafel equation

$$J_s^{\text{Li}} = -J_{s0}^{\text{Li}} \exp\left(-\frac{\alpha_s^c n F}{RT} \eta_s\right) \quad [21]$$

where the overpotential η_s of the parasitic reaction is defined as

$$\eta_s = \phi_n^1 - U_s^{\text{OCP}} - J_n S_n R_n^f \quad [22]$$

The total current density (J_n) at the negative electrode is the sum of the intercalation/deintercalation current density and the parasitic reaction current density.

$$J_n = J_n^{\text{Li}} + J_s^{\text{Li}} = \frac{I_{\text{app}}}{S_n} \quad [23]$$

The electronic charges are completely consumed by the intercalation/deintercalation of lithium ions at the Li_xCoO₂ positive electrode.

$$J_p = J_p^{\text{Li}} = \frac{I_{\text{app}}}{S_p} \quad [24]$$

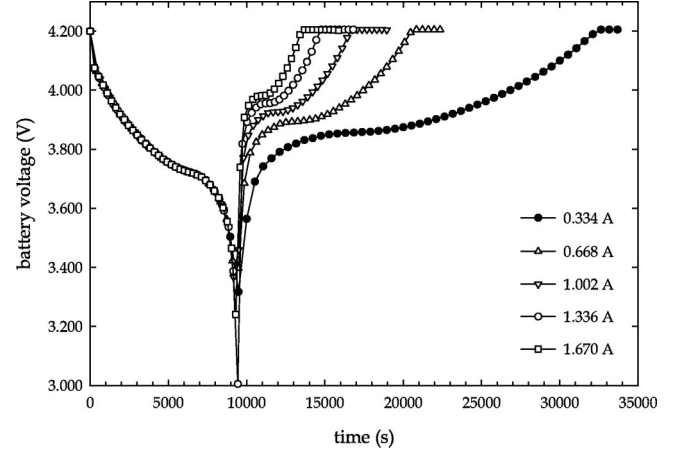
For the next discharge process, the dimensionless lithium concentration (\bar{C}_{i0}^{Li}) at the beginning of the discharge-charge cycle is used as the initial condition for the diffusion equation in the solid phase. The surface film resistance (R^f) used in the BV and Tafel equations are modified based on the loss of lithium ions due to the parasitic reaction in the previous cycle.

The loss of the active lithium was estimated using the following equation

$$Q_s = \int_{t=0}^{t=T_s} J_s^{\text{Li}} S_n dt \quad [25]$$

Table II. Parameters for the electrochemical parasitic reaction

Parameter	Units	Value
U_s^{OCP}	V	0.4
M	g/mol	100
ρ	g/cm ³	2.1
J_s^{Li}	A/cm ²	0.75×10^{-11}
κ	S/cm	0.5×10^{-7}

**Figure 2.** Simulation of initial voltage profile (simulation of capacity check; applied discharge current of 0.835 A).

Due to the parasitic reaction, the dimensionless lithium concentration (\bar{C}_{i0}^{Li}) at the beginning of the discharge-charge cycle at cycle number ($N + 1$) at the MCMB electrode is less than that at cycle number N and it is given by

$$\bar{C}_{n0}^{\text{Li}}|_{N+1} = \bar{C}_{n0}^{\text{Li}}|_N - \bar{Q}_s|_N \quad [26]$$

where dimensionless loss in concentration of lithium in MCMB electrode ($\bar{Q}_s|_N$) is expressed as

$$\bar{Q}_s|_N = \frac{Q_s|_N}{\varepsilon_n F V_n C_n^{\max}} \quad [27]$$

Continuous precipitation of insoluble product (LiCH₂CH₂OCO₂Li↓) on the surface of the negative electrode causes the resistance of the film to increase with the increase of the cycle number. Thus

$$R_{s|N+1}^f = R_{s|N}^f + R_s|_N \quad [28]$$

where the resistance of the insoluble product at cycle number N ($R_s|_N$) is a function of film thickness (δ_f)

$$R_s|_N = \frac{\delta_{f|N}}{\kappa} \quad [29]$$

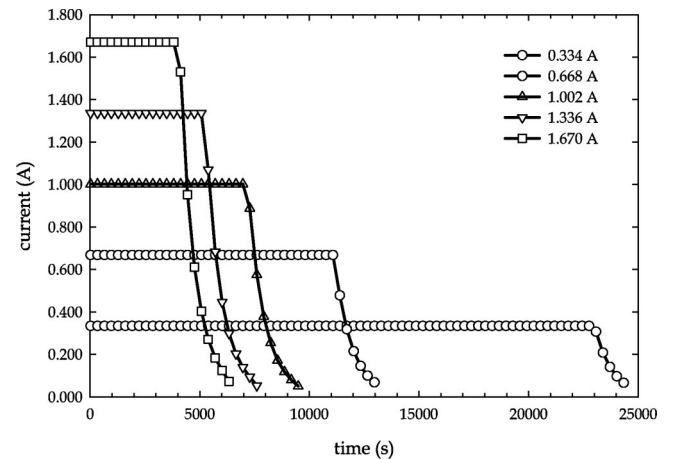
**Figure 3.** Initial charge current profiles.

Table III. Influence of CR on charge-discharge performance.

CR (A)	CC capacity (Ah)	CV capacity (Ah)	Discharge capacity (Ah)	CC charging time (s)	CV charging time (s)	Total charging time (s)
0.334	2.123	0.075	2.188	22,905	1663	24,568
0.668	2.055	0.145	2.188	11,095	2126	13,221
1.002	1.992	0.208	2.188	7179	2316	9495
1.336	1.930	0.27	2.188	5221	2400	7621
1.670	1.875	0.324	2.188	4063	2421	6484

Volume balance of the precipitated insoluble product on the surface of MCMB negative electrode yields

$$\frac{\partial \delta_{fN}}{\partial t} = -\frac{J_s^{Li} \times M}{\rho \times F} \quad [30]$$

To estimate the capacity or the discharge performance at a specified cycle number, the diffusion equations in the solid phase were solved first in order to determine the value of the dimensionless concentration of lithium at the solid/electrolyte interface \bar{C}_i^{Li-S} . Next, this value was substituted into the BV equation in order to solve for the potential in the solid phase of the positive and negative electrode. During the CV charging process, a trial and error method was used to solve the continuous decay of the current.

The loss of active lithium ions and the rise in the surface film on the negative electrode were estimated using Tafel Eq. 21. The dimensionless lithium concentration at the beginning of the discharge-charge cycle \bar{C}_{n0}^{Li} and the surface film resistance R^f at the negative electrode were modified at the beginning of every discharge-charge cycle according to Eq. 26 and 28. The diffusion equation was solved numerically using the Crank-Nicolson method¹⁵ to ensure the local truncation error at any time is on the order of $o((\Delta r)^2 + (\Delta t)^2)$ in the computations. The simulations were carried out on a Compaq Visual Fortran platform. A band-structure subroutine developed by us was repeatedly called to expedite the computations. The parameters used in the simulations are presented in Tables I and II.

Results and Discussion

Simulation of charge-discharge characteristics.—Figures 2 and 3 present the simulations of the cell voltage and the cell current as a function of charge/discharge time, respectively. The simulations were carried out for the initial CC-CV charging and CC discharging cycle. The cell voltage shown in Fig. 2 is the difference of the solid phase potential (ϕ^1) between the positive end ($X = 0$) and the negative end ($X = L$) of the Li-ion battery. The charge currents in Fig. 3 were varied from 0.334 to 1.670 A. The total charge capacity

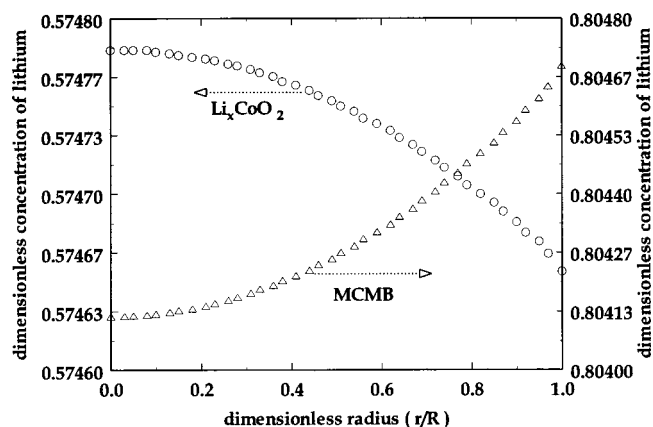


Figure 4. Concentration profiles of lithium inside particles of Li_xCoO_2 and MCMB (21 s from the beginning of the CV charge process; CR: 0.334 A).

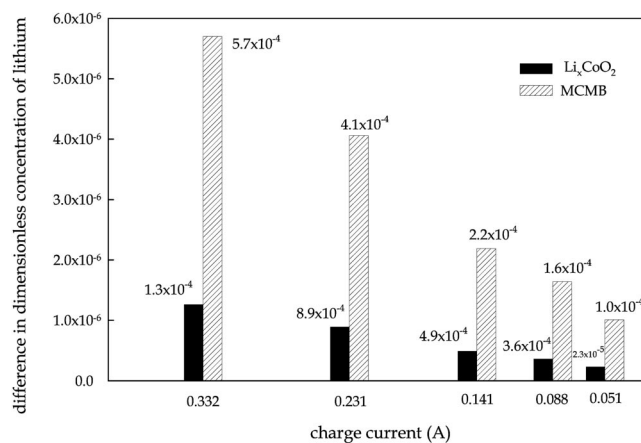


Figure 5. $|C^{Li}(\bar{r} = 1) - C^{Li}(\bar{r} = 0)|$ vs. time inside particles of Li_xCoO_2 and MCMB.

was supplied by using CC-CV charging protocol. As shown in Fig. 3, the model predicts a decrease in CC charging time with an increase of charging current.

The results shown in Table III indicate that the CV charging supplies between 3.4 and 14.8% of the total charge capacity depending upon the charge rates used. A charging current of 0.334 A results in CC capacity of almost 96.6% of the total charge capacity. Despite the observed differences in the charge characteristics when different charge rates were used to charge the battery, the initial discharge curve as well as the discharge capacity shown in Fig. 2 remain identical.

Figure 4 shows the concentration profile of lithium inside the Li_xCoO_2 and MCMB particles 21 s after the beginning of CV charging. The model predicts a positive concentration gradient inside the MCMB negative electrode. As expected, a negative concentration gradient is observed inside the positive electrode.

The dependence of lithium concentration in both electrodes as a function of applied charge current in CV charging mode is shown in Fig. 5. The concentration gradient becomes gradually smaller as CV charging time increases, indicating that lithium ions continue to diffuse from the Li_xCoO_2 positive electrode to MCMB negative electrode until the current reaches the cutoff current of 50 mA. The dimensionless concentration of lithium at the MCMB/electrolyte interface ($\bar{r} = 1$) increases while it decreases at the Li_xCoO_2 /electrolyte interface with increasing the CV charging time.

Simulation of cycling characteristics.—Figure 6 shows cycling

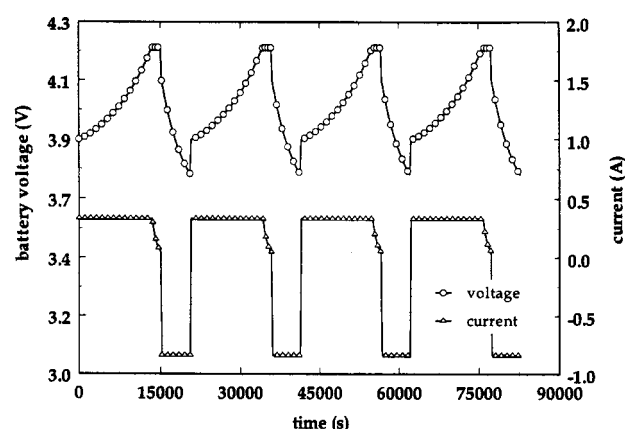


Figure 6. Simulations of the first four charge-discharge cycles (CR: 0.334 A, discharge current: 0.835 A, EOCV: 4.2 V, DOD: 0.6).

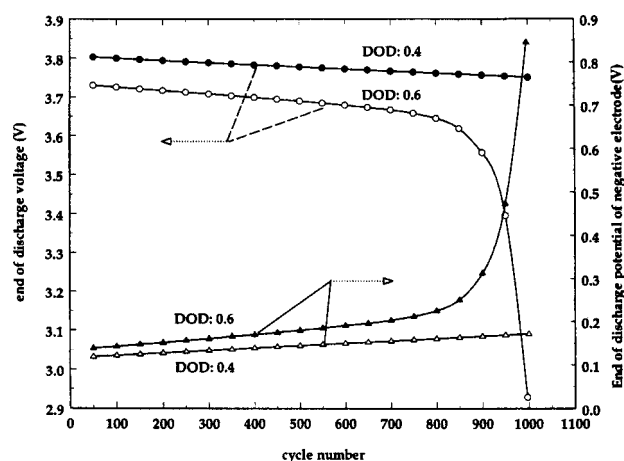


Figure 7. End of discharge voltage and end of discharge potential of negative electrode vs. cycle number.

simulations for the first four cycles. The simulations were performed for EOCV of 4.2 V and DOD of 0.6. Because a low current of 0.334 A (C/5 rate) is used to charge the battery, the CC charging is predominant. As a result of capacity fade, a gradual decrease is observed for the end of discharge voltage. Because the model controls the DOD by controlling the discharge time, it can be used for cycle life predictions when the battery is cycled to different DOD.

Figure 7 shows the end of cell discharge voltage and the end of discharge potential of the negative electrode as a function of cycle number simulated for DOD of 0.4 and 0.6. When the battery is charged to EOCV of 4.2 V and discharged to DOD of 0.4, the end of discharge voltage up to 950 cycles is higher than 3.7 V, which agrees with the experimental results. For DOD of 0.6, the end of discharge voltage decreases gradually up to 800 cycles. After 800 cycles it drops rapidly for less than 150 cycles to a level which is lower than 3.0 V.

The end of discharge voltage corresponding to DOD of 0.4 is always higher than that corresponding to DOD of 0.6 for the same cycle number. It is necessary for the battery to be cycled to more cycles in order for the end of discharge voltage to reach the cutoff voltage of 3.0 V. The output voltage of the battery is determined by the difference between the solid phase potential of the positive and the negative electrode. Both potentials are a function of the solid phase concentration of lithium inside the particles. Because of a continuous consumption of the active lithium ions due to the parasitic reaction, the dimensionless lithium concentration at the beginning of the discharge-charge cycle at the negative electrode de-

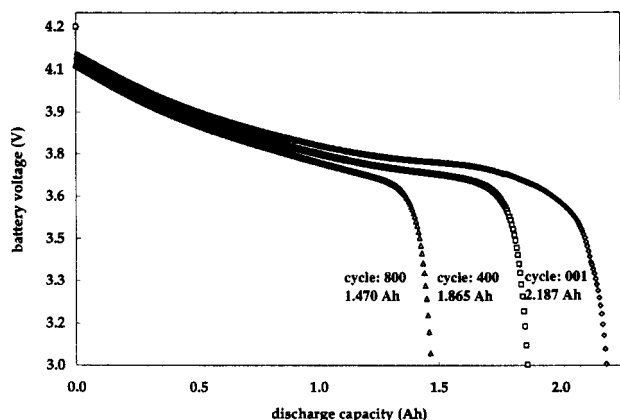


Figure 8. Discharge voltage profile at different cycle numbers at discharge current of 0.835 A (EOCV: 4.2 V, DOD: 0.6).

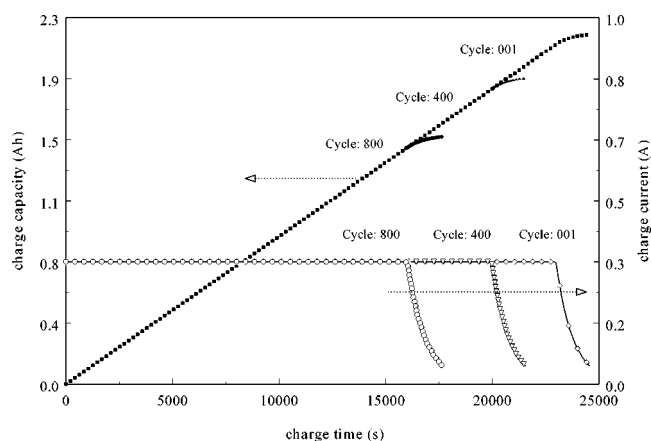


Figure 9. Charge capacity and charge current at different cycle numbers at charge current of 0.334 A (EOCV: 4.2 V, DOD: 0.6).

creases gradually according to Eq. 26. After 800 cycles, when the battery is cycled to DOD of 0.6, almost all active lithium depletes from the negative electrode, causing the state of charge (SOC) at the end of discharge to be close to 0%. As shown in Fig. 7, the potential of the negative electrode rises rapidly from a plateau which is initially lower than 0.2 V to a potential which is higher than 0.8 V at 800 cycles. The observed large increase of the potential of the negative electrode due to irreversible loss of the active lithium ions causes the battery to fail. As shown in Fig. 8, the capacity of the battery after 800 cycles decreases to 1.470 Ah from an initial 2.187 Ah.

The lithium-ion concentration in the negative electrode at the beginning of discharge simulated for DOD of 0.4 decreases at a slower rate than the rate observed for DOD of 0.6. The simulations indicated that only when the battery is cycled up to 1400 cycles with DOD of 0.4 does it reach the same lithium depletion state observed for 800 cycles when DOD of 0.6 was used to cycle the battery.

Simulation of capacity check.—Using Eq. 26-28, the model continuously updates the dimensionless lithium concentration at the beginning of the discharge-charge cycle (\bar{C}_{n0}^{Li}) as well as the surface film resistance (R^f) values for every cycle. These parameters control the capacity loss and the voltage profile of the battery.

Figure 8 shows simulated discharge curves after 1, 400, and 800 cycles. The battery was cycled with CR of 0.334 A, EOCV of 4.2 V, and DOD of 0.6. Due to the parasitic reaction, dimensionless lithium concentration at the beginning of a discharge-charge cycle decreases while the capacity loss increases with the cycle number. The voltage

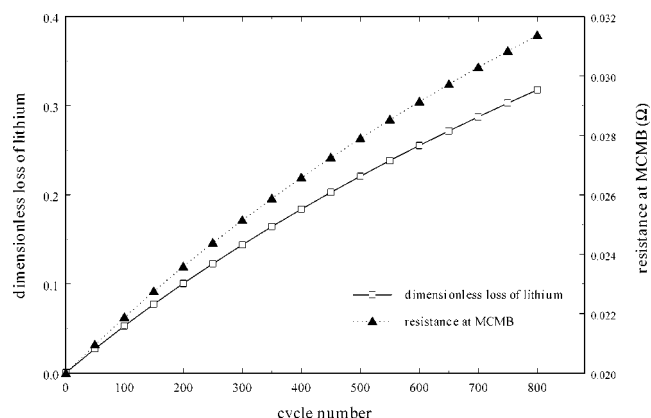


Figure 10. Dimensionless loss of lithium (\bar{Q}_s) and total resistance at MCMB negative electrode (R^f) vs. cycle number (EOCV: 4.2 V, DOD: 0.6).

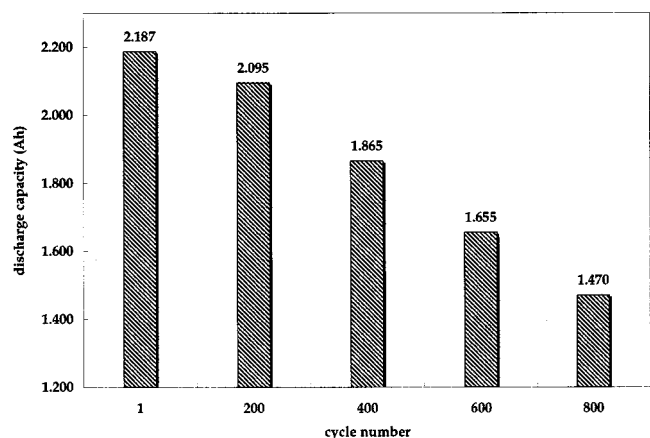


Figure 11. Simulated discharge capacity vs. cycle number.

plateau of simulated discharge curves continues to decrease, which is attributed to the continuous increase of the film resistance as a result of the parasitic reaction.

Figure 9 shows simulated charge curves for cycles 1, 400, and 800. The current profiles for different cycles are also given for comparison. As shown in Fig. 9, the CC part of charging capacity decreases with the cycle number. Similar experimental results were observed in our previous study.¹⁶ The variation of both the dimensionless loss of lithium (\bar{Q}_s) and the film resistance on the surface of the negative electrode (R^f) vs. cycle number are shown in Fig. 10. The parasitic reaction causes the dimensionless lithium concentration at the beginning of discharge-charge cycle to decrease, while the film resistance increases with the increase of the cycle number. Figure 11 summarizes the discharge capacity values as a function of cycle number. The simulations were performed for EOCV of 4.2 V, DOD of 0.6, and CR of 0.334 A.

Influence of EOCV and DOD on cycle life.—EOCV and DOD control the cycle life of the battery.¹⁰ Overcharging the lithium-ion battery above 4.2 V results in a significant loss in capacity and triggers safety concerns.⁶ For EOCV lower than 4.2 V, the cell is partially charged. Figure 12 shows the influence of different EOCV values on the capacity loss during cycling. The data were obtained by simulating the performance of the battery discharged to DOD of 0.6. The simulated EOCVs were 4.0 and 4.2 V. The simulation results indicated that the capacity fade was higher for EOCV of 4.2 V.

The dependence of the capacity loss on EOCV and DOD are given by Eq. 21 and 25. The OCP for the parasitic reaction was set to be 400 mV.¹³⁻¹⁴ The parasitic reaction takes place only when the

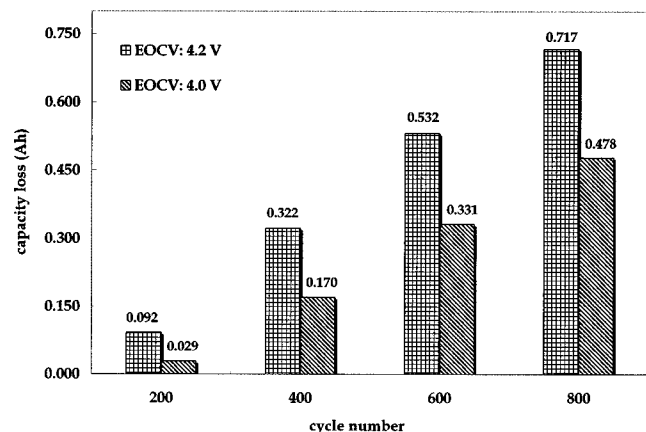


Figure 12. Influence of EOCV on discharge capacity (DOD: 0.6).

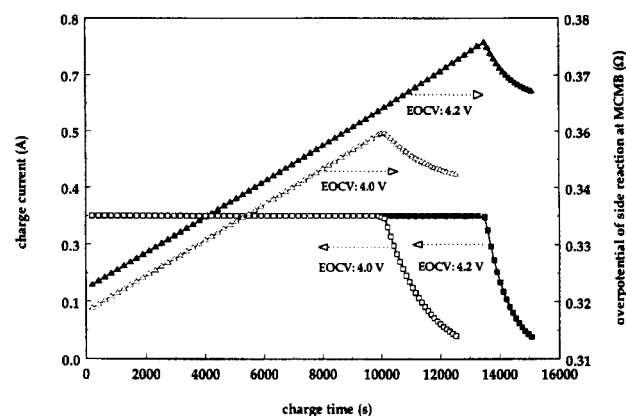


Figure 13. Overpotential vs. charge time in cycle 2 at different EOCV values DOD: 0.6).

overpotential determined by Eq. 11 is more cathodic than this potential. Our simulation results indicated that when the battery is initially charged from 100% DOD to fully charged state, the potential of the negative electrode varies in the range between 250 and 50 mV. Thus, the parasitic reaction occurs regardless of the starting charging potential. The total charging time and consequently the total time for the parasitic reaction are functions of EOCV and DOD. The overpotential and the total time of the parasitic reaction in the second cycle presented in Fig. 13 increases with an increase of EOCV. The overpotential of the negative electrode increases with the increase of the EOCV and shows a maximum at the transition point from CC to CV charging. The observed decrease of the overpotential in Fig. 13 results from a fast decay of the current when the battery is in CV charging mode. The voltage drop due to the surface film resistance described in Eq. 22 is proportional to the charging current and to the surface film resistance at the negative electrode. Figure 14 shows that both the dimensionless loss of lithium and the surface film resistance increase with the increase of cycle number.

A depth of discharge (DOD) is defined as the level to which a battery voltage is discharged and is generally calculated in reference to the initial discharge capacity of the battery. For example, a 100% DOD for a 2.187 Ah rechargeable lithium-ion battery means the battery should be discharged to the point where discharge capacity is exactly 2.187 Ah. The influence of DOD on overpotential is shown in Fig. 15. In this simulation the EOCV was set to be 4.2 V while the DOD was set at 0.4 and 0.6. The observed fast capacity fade shown in Fig. 15 when the battery is cycled to DOD of 0.6 results from

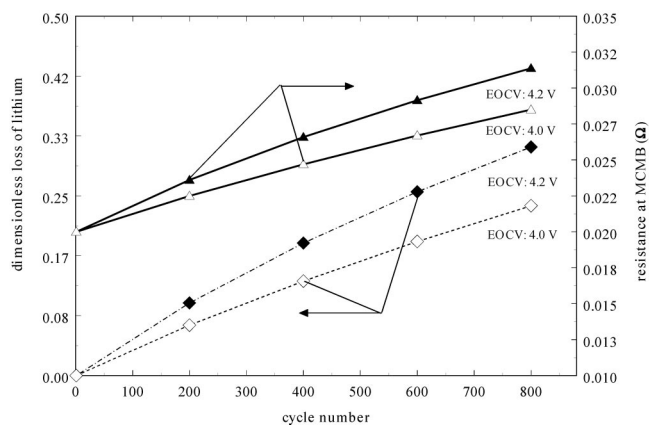


Figure 14. Dimensionless loss of lithium (\bar{Q}_s) and total resistance at MCMB negative electrode (R^f) vs. cycle number at different EOCV values (DOD: 0.6).

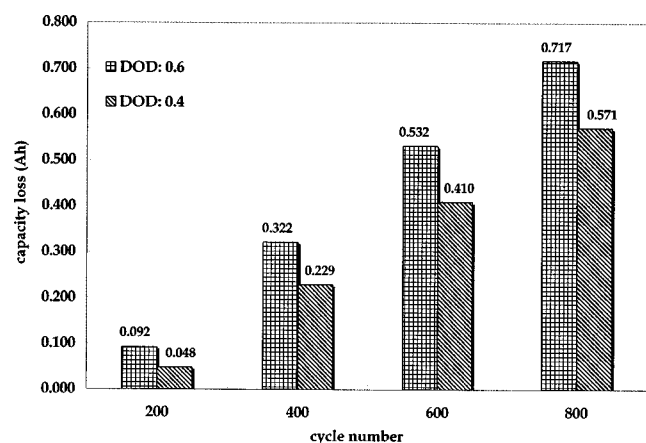


Figure 15. Influence of DOD on discharge capacity (EOCV: 4.2 V).

longer parasitic reaction time (Eq. 25) when compared to DOD of 0.4. The DOD controls the kinetics of the parasitic reaction by controlling the duration of the parasitic reaction as well as the overpotential of the parasitic reaction shown in Fig. 16.

Influence of exchange current density of parasitic reaction (J_{s0}^{Li}) and conductivity (κ) on capacity fade.—The exchange current density of the parasitic reaction (J_{s0}^{Li}) and the conductivity of the surface film on the MCMB electrode (κ) were assumed in our simulations. No attempt was made in this paper to estimate the accurate values for these two parameters. A comparison of the capacity fade of a battery after 500 cycles with different values of J_{s0}^{Li} is shown in Fig. 17. The cycling simulation was performed by charging the battery to EOCV of 4.2 V and discharging it to DOD of 0.6. The capacity fade after 500 cycles increases with increase of the exchange current density for the parasitic reaction. The simulation results clearly show that the loss of the active lithium \bar{Q}_s increases with the increase of the exchange current density of the parasitic reaction. The surface film resistance R^f on the MCMB negative electrode as a function of cycle number follows a similar trend.

Similar simulations were carried out to analyze the effect of the conductivity of the newly formed surface film on charge/discharge performance of the battery. The simulations were carried out by charging the battery to EOCV of 4.2 V and discharging it to DOD of 0.6 for different values of conductivity (i.e., 0.5×10^{-8} , 0.1×10^{-8} , 0.5×10^{-7} S/cm). The simulation results indicated that the voltage plateau is higher, and the total charging time as well as the CC charging time become longer by lowering the film con-

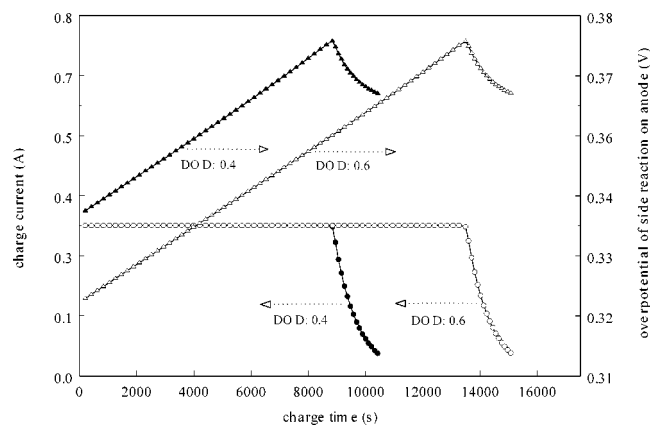


Figure 16. Overpotential vs. charging time in cycle 2 under different DOD values (EOCV: 4.2 V).

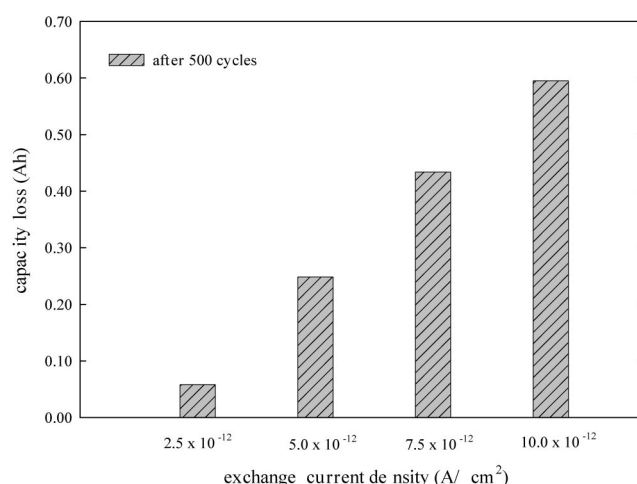


Figure 17. Influence of exchange current density of the parasitic reaction (J_{s0}^{Li}) on the capacity fade.

ductivity. However, no change in capacity was observed in spite of the differences in the current/voltage profiles in charging/discharging. Thus, the difference in the surface film resistance on the MCMB electrode due to different conductivity values is not related to the capacity fade with cycling. These results are in agreement with those observed by Christensen and Newman.⁷

Conclusion

A charge-discharge capacity fade model was developed based on the loss of active lithium ions due to solvent reduction reaction. The rise in the surface film resistance at anode due to the precipitation of insoluble product of the parasitic reaction was also considered in the model. The model considers process parameters such as CR, DOD, and EOCV and controls the required DOD by controlling the discharge time and estimates the discharge voltage as a function of cycle number. The results indicated that both the dimensionless loss of lithium and the surface film resistance increase with the increase of the overpotential and the duration of the parasitic reaction. The loss of the active lithium \bar{Q}_s also increases with the increase of the exchange current density of the parasitic reaction. The total parasitic reaction time increases with an increase of EOCV or DOD. The overpotential of the parasitic reaction at the negative electrode increases with an increase of EOCV and shows a maximum at the transition point from CC to CV charging.

Acknowledgments

Financial support provided by the National Reconnaissance Office for Hybrid Advanced Power Sources no. NRO-00-C-1034 is acknowledged gratefully.

The University of South Carolina assisted in meeting the publication costs of this article.

List of Symbols

a	specific surface area of porous electrode, cm^2/cm^3
C_1^{Li}	solid phase concentration of lithium, mol/cm^3
C_1^{Li-S}	solid phase concentration of lithium at electrode/electrolyte interface, mol/cm^3
C_1^{max}	solid phase concentration of lithium when the stoichiometric coefficient x in Li_xCoO_2 or y in Li_xC or is equal to 1, mol/cm^3
D	diffusion coefficient, cm^2/s
F	Faraday's constant, 96,487 C/mol
I	current, A
J_i	faradaic current across the electrode/electrolyte interface, A/cm^2
J_{i0}^{Li}	current density for intercalation reaction, A/cm^2
J_{i0}^{Li}	exchange current density for intercalation reaction, A/cm^2
J_s^{Li}	exchange current density for parasitic reaction, A/cm^2
I_{app}	applied current density, A
k	rate constant of intercalation/deintercalation, $A/cm^2/(mol/cm^3)^{0.5}$
M	molecular weight, g/mol

V volume of electrode, cm^3
 Q_s capacity lost due to parasitic reaction, Ah
 r radial coordinate, cm
 R universal gas constant, 8.314 J/mol
 R_p radius of particles, cm
 R^i total resistance at MCMB electrode, Ω
 R_C initial constant resistance at MCMB electrode, Ω
 R_S resistance of newly formed film, Ω
 S superficial surface area, cm^2
 t time, s
 T temperature, 298.15 K
 T_S total parasitic reaction time, s
 U local equilibrium potential, V
 X thickness of the battery, m
 x stoichiometric coefficient in Li_xCoO_2 or Li_xC_6

Greek

α^a, α^c anodic and cathodic transfer coefficients of electrochemical reaction
 ε volume fraction of a solid phase
 ϕ potential of a phase, V
 η overpotential of electrochemical reaction, V
 κ conductivity of the newly formed surface film, S/cm
 θ active sites on the surface of the electrode
 ρ density of active material, g/cm^3
 δ film thickness, cm

Subscript or Superscripts

1 solid phase
 2 liquid phase
 C constant
 f surface film on the particles
 i positive or negative electrode
 n negative electrode
 N cycle number

p positive electrode
 S parasitic reaction
 0 initial state
 Li lithium in solid phase
 Li^+ lithium in liquid phase
 - dimensionless variables

References

1. T. Inoue, T. Sasaki, N. Imamura, H. Yoshida, and M. Mizutani, *NASA Aerospace Battery Workshop*, Huntsville, AL (2001).
2. I. Bloom, B. W. Cole, J. J. Sohn, S. A. Jones, E. G. Polzin, V. S. Battaglia, G. L. Henriksen, C. Motloch, R. Richardson, T. Unkelhaeuser, D. Ingersoll, and H. L. Case, *J. Power Sources*, **101**, 238 (2001).
3. M. Broussely, S. Hereyre, P. Biensan, P. Kasztejna, K. Nechev, and R. J. Staniewicz, *J. Power Sources*, **97-99**, 13 (2001).
4. R. Darling and J. Newman, *J. Electrochem. Soc.*, **145**, 990 (1998).
5. R. Spotnitz, *J. Power Sources*, **113**, 72 (2002).
6. P. Ramadass, B. Haran, R. E. White, and B. N. Popov, *J. Power Sources*, **123**, 230 (2003).
7. J. Christensen and J. Newman, *J. Electrochem. Soc.*, **150**, A1416 (2003).
8. M. Doyle, T. F. Fuller, and J. Newman, *J. Electrochem. Soc.*, **140**, 1526 (1993).
9. G. Ning and B. N. Popov, *J. Power Sources*, **117**, 160 (2003).
10. P. Ramadass, B. Haran, P. M. Gomadam, R. E. White, and B. N. Popov, *J. Electrochem. Soc.*, **151**, A196 (2004).
11. D. Aurbach, E. Zinigrad, Y. Cohen, and H. Teller, *Solid State Ionics*, **148**, 405 (2002).
12. D. Aurbach, A. Zaban, Y. Ein-Eli, I. Weissman, O. Chusid, B. Markovsky, M. Levi, E. Levi, A. Schechter, and E. Granot, *J. Power Sources*, **68**, 91 (1997).
13. D. Aurbach, *J. Power Sources*, **89**, 206 (2000).
14. Y.-G. Ryu and S.-I. Pyun, *J. Electroanal. Chem.*, **97**, 433 (1997).
15. J. B. Riggs, *An Introduction to Numerical Methods for Chemical Engineers*, 2nd ed., p. 216, Texas Tech University Press, Lubbock, TX (1994).
16. P. Ramadass, B. Haran, R. White, and B. N. Popov, *J. Power Sources*, **111**, 210 (2002).